Nanoscale

Enhanced Carrier Transport by Transition Metal Doping in WS2 Field Effect Transistors

Journal:	*Nanoscale*
Manuscript ID	NR-ART-02-2020-001573.R1
Article Type:	Paper
Date Submitted by the Author:	12-Apr-2020
Complete List of Authors:	Liu, Maomao; University at Buffalo - The State University of New York Wei, Sichen; University at Buffalo - The State University of New York Shahi, Simran; University at Buffalo - The State University of New York Jaiswal, Hemendra; University at Buffalo - The State University of New York Paletti, Paolo; University of Notre Dame Fathipour, Sara; University of Notre Dame Remskar, Maja; Jozef Stefan Institute Jiao, Jun; Portland State University, Mechanical and Materials Engineering Hwang, Wansik; Korea Aerospace University Yao, Fei; University at Buffalo - The State University of New York Li, Huamin; University at Buffalo - The State University of New York, Electrical Engineering

Enhanced Carrier Transport by Transition Metal Doping in WS_2 Field Effect Transistors

Maomao Liu,[1] Sichen Wei,[2] Simran Shahi,[1] Hemendra Nath Jaiswal,[1]

Paolo Paletti,[3] Sara Fathipour,[3] Maja Remskar,[4] Jun Jiao,[5]

Wansik Hwang,[6†] Fei Yao,[2†] and Huamin Li[1†]

[1] Department of Electrical Engineering, University at Buffalo, the State University of New York, Buffalo, NY 14260, USA

[2] Department of Materials Design and Innovation, University at Buffalo, the State University of New York, Buffalo, NY 14260, USA

[3] Department of Electrical Engineering, University of Notre Dame, South Bend, IN 46556, USA

[4] Department of Solid State Physics, Jozef Stefan Institute, Ljubljana, 1000, Slovenia

[5] Center for Electron Microscopy and Nanofabrication, Portland State University, Portland, OR 97207, USA

[6] Department of Materials Engineering, Korea Aerospace University, Goyang 10540, Republic of Korea

---

[†] Corresponding authors: whwang@kau.ac.kr, feiyao@buffalo.edu, huaminli@buffalo.edu

Abstract

High contact resistance is one of the primary concerns for electronic device applications of two-dimensional (2D) layered semiconductors. Here, we explore the enhanced carrier transport through metal-semiconductor interfaces in WS_2 field effect transistors (FETs) by introducing a typical transition metal, Cu, with two different doping strategies: (i) a "generalized" Cu doping by using randomly distributed Cu atoms along the channel and (ii) a "localized" Cu doping by adapting an ultrathin Cu layer at the metal-semiconductor interface. Compared to the pristine WS_2 FETs, both the generalized Cu atomic dopant and localized Cu contact decoration can provide a Schottky-to-Ohmic contact transition owing to the reduced contact resistances by 1 – 3 orders of magnitude, and consequently elevate electron mobilities by 5 – 7 times higher. Our work demonstrates that the introduction of transition metal can be an efficient and reliable technique to enhance the carrier transport and device performance in 2D TMD FETs.

KEYWORDS: 2D materials, WS_2, transition metal, transistor, carrier transport

Tungsten disulfide (WS_2) with a semiconducting 2H phase is one of two-dimensional (2D) transition metal dichalcogenides (TMDs) exhibiting a series of unique properties, such as strong spin-orbit coupling, band splitting, and high nonlinear susceptibility[1-3]. Especially for future nanoelectronic applications, WS_2 stands out as a promising channel material compared to other 2D semiconductors. For example, WS_2 has a direct bandgap of 1.4 – 2.0 eV[4-7] for the monolayer and an indirect bandgap of 1.2 – 1.3 eV[4-6] for the bulk crystals. The carrier mobility of WS_2 has been theoretically predicated up to ~5,300 cm^2/Vs at 77 K[8] and ~700 – 1,100 cm^2/Vs at room temperature[8,9], which exceeds most of the commonly used semiconducting TMDs such as MoS_2 (340 cm^2/Vs), $MoSe_2$ (240 cm^2/Vs), WSe_2 (705 cm^2/Vs), owing to the relatively small effective

mass ($0.34m_0$ for electrons and $0.46m_0$ for holes, where m_0 is the free electron mass)[7]. Although the experimentally demonstrated electron mobilities, limited by Coulomb impurities, charge traps, surface defects and roughness, are much lower than the theoretical predication, new techniques have been developed to practically improve the mobility, for example, by exploiting *h*-BN[10] or high-*k*[11] dielectrics. For the application of field-effect transistors (FETs), monolayer WS_2 FETs are predicated to outperform other TMD FETs in terms of the on-state current density ($J_{D,on}$) for both p- and n-type transistors (~2,800 μA/μm for the monolayer WS_2 versus 2,200 – 2,400 μA/μm for the monolayer MoS_2, $MoSe_2$, and $MoTe_2$ FETs)[11]. In addition to the carrier mobility, the pristine hysteresis width of WS_2 during reliability tests is the lowest compared to MoS_2, $MoSe_2$ and $MoTe_2$ FETs[12]. The current on/off ratio at room temperature has been experimentally demonstrated up to ~10^6 for the monolayer WS_2 FETs[13,14] and to ~10^8 for the multilayer WS_2 FETs[15]. A nearly ideal subthreshold swing (SS) of 70 mV/decade at room temperature has been demonstrated in a simple back-gated WS_2 FET through a 10-nm-thick SiO_2 layer[16]. To further break the thermal limit of the SS, various WS_2-based vertical transistors operated by a band-to-band Zener tunneling mechanism have been investigated, including Gr/WS_2/Gr[17] and WS_2/SnS_2[18] van der Waals (vdW) heterostructures where Gr is the monolayer or multilayer graphene.

To fully explore the potential of WS_2 as the semiconducting channel material for the nanoelectronic device applications, the manipulation and improvement of its physical properties especially the carrier transport is highly required. For example, substitutional doping can occur as direct substitution of atoms in the lattice or into interstitial sites between existing atoms in the lattice. Owing to the unique nature of the vdW gaps, the atomic dopants in 2D materials can also intercalate between the layers, resulting in the changes in morphologic, electronic, optical, magnetic, and catalytic properties etc[19,20]. Compared to group XI elements such as Ag and Au

which are widely used for wire-bonding, interconnects, and electrode materials, Cu as a representative transition metal has been demonstrated to effectively shift the Fermi level (E_F) up to the minima of the conduction band edge (E_C) and induce an n-type doping on black phosphorus (BP, or phosphorene), owing to its low electronegativity which can easily donate its 4*s* electron to BP[21,22]. The Cu doping effect on other 2D materials, such as graphene[23], MoS_2[24,25], $MoSe_2$[25], Bi_2Se_3[26-28], $ZrSe_2$[29], $SnSe_2$[30], and SnS[31] etc. have also been investigated. Especially for WS_2, Cu can serve as an effective dopant to induce a microscopic ferromagnetic development which originates from the *p-d* hybridization between the Cu dopant and its neighboring S atoms and consequently the splitting of the energy levels near E_F[32]. However, the impact of Cu doping on the electronic carrier transport of WS_2 has not been explored experimentally yet. Furthermore, considering the wide applications of Cu as transistor contacts and interconnects in current semiconductor technology, the metal-semiconductor contact condition at the Cu/WS_2 interface critically limits the carrier injection and collection efficiency during the transistor operation, especially for the extremely-scaled short-channel devices where the contacts play a more important role in the carrier transport and device performance[33,34]. Therefore, an understanding of Cu/WS_2 contact can be one of the keys to achieve the full performance potential of the emerging WS_2 transistors.

In this work, we experimentally reveal the impact of Cu doping on the carrier transport of WS_2 through the metal-semiconductor interfaces, and statistically evaluate the transistor performance. Specifically, Cu as the representative transition metal is introduced using two different techniques. In the Cu-doping technique, Cu is randomly distributed into the WS_2 crystals during the synthesis and acts as "generalized" n-type atomic dopants within the channel. Whereas in the Cu-contact technique, Cu is deposited as an ultrathin contact decoration layer on the WS_2

surface and provides a "localized" doping effect only at the metal-semiconductor interface. A schematic illustration of these two doping strategies and the corresponding electron transport through the metal-semiconductor interfaces is shown in. Compared to the pristine WS_2 FETs, both the Cu-doped and Cu-contact WS_2 FETs show a clear Schottky-to-Ohmic contact improvement, due to a significant reduction of the Schottky barrier (about 28% to 60% lower) and thus the contact resistance (over 1 to 3 orders of magnitude lower). The enhanced carrier transport can be attributed to the charge transfer with Cu which changes the Fermi level (by ~0.11 eV) of WS_2 along the channel for the Cu-doped devices, or reduces the workfunction of Cu (by ~0.41 eV) at the metal-semiconductor interface for the Cu-contact devices. In addition, we carry out a statistical study by testing about 30 devices for each type of the WS_2 FETs, and demonstrate the improvement of the transistor performance including field effect mobility (μ_{FE}), on/off ratio, $J_{D,on}$, and SS. Our results suggest that, owing to the doping effect, the transition metal Cu either as the generalized atomic dopant or the localized contact decoration can effectively enhance the carrier transport and device performance for 2D semiconducting WS_2.

RESULTS AND DISCUSSION

Output characteristics. For a comparative study, we fabricate three types of typical global-back-gate transistors: pristine, Cu-doped, and Cu-contact WS_2 FETs, as shown in **Fig. S1** in Supplementary Information. Compared to the pristine WS_2 FET which is the control sample in this work, the Cu-doped WS_2 FETs include Cu as the generalized atomic dopants during the WS_2 crystal synthesis. Both the pristine and Cu-doped WS_2 FETs have Ti/Au (10 nm/100 nm) deposited as source and drain electrodes. The Cu-contact WS_2 FETs have Cu/Ti/Au (2 nm/10 nm/100 nm) as the electrodes on the pristine WS_2 flakes where the thin Cu layer serves as a

localized contact decoration at the metal-semiconductor interface. A comparison of drain current density versus drain voltage (J_D-V_D) output characteristics at various gate voltages (V_G) for all three types of the devices is performed at room temperature, as shown in **Fig. 1**. The pristine WS_2 FET possesses non-linear current-voltage (IV) characteristics at low V_D, suggesting a large Schottky barrier at the metal-semiconductor contacts. In contrast, the Cu-doped WS_2 FET indicates a linear IV relation and thus an Ohmic contact at low V_D. Meanwhile, current saturation is clearly obtained in the Cu-doped device, for example, at V_D of 2 V for V_G of 30 V. Similar to the Cu-doped WS_2 FET, the Cu-contact WS_2 FET also shows the Ohmic contact and current saturation, but the maximum $J_{D,on}$ is increased significantly up to 42 μA/μm at V_D of 5 V and V_G

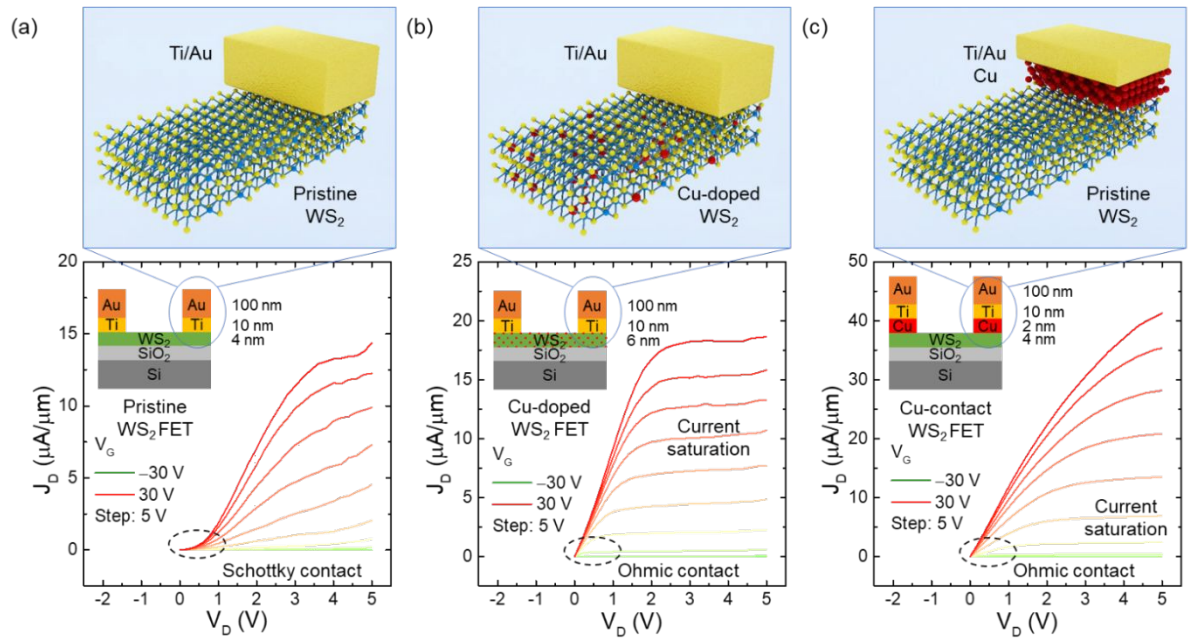

Fig. 1 Comparison of output characteristics of WS_2 FETs. (a, b, c) The output characteristics of pristine, Cu-doped, and Cu-contact WS_2 FETs at various V_G (from –30 to 30 V with a step of 5 V) at room temperature, respectively. Inset: Schematic illustration of the device structures and the corresponding metal-semiconductor interfaces.

of 30 V.

To further understand the carrier transport properties, the output characteristics at the on state (V_G = 30 V) are replotted in various analytical models, as shown in **Fig. S2** in Supplementary Information. In the log(J_D) versus $V_D^{1/2}$ curves (see **Fig. S2 (a)**), a linear dependence is found at V_D > 2 V for all three types of the devices, suggesting that the carrier injections subject to the Schottky emission at room temperature[35] which is described as

$$J_D \propto exp\left[\frac{-\left(\phi_b - \sqrt{\frac{q^3 V_D}{L\pi\varepsilon_0\varepsilon_r}}\right)}{k_B T}\right] \qquad (1).$$

Here ϕ_b is the barrier height, q is the electronic charge, ε_0 is the permittivity of the vacuum, ε_r is the relative permittivity of WS_2, L is the channel length, k_B is the Boltzmann constant, and T is the temperature. Due to the identical channel material, both the pristine and Cu-contact devices possess the similar slopes (0.29 and 0.31) compared to that of the Cu-doped device (0.03). The smaller slope of the Cu-doped device also indicates a larger ε_r after the generalized Cu doping in WS_2. **Equation 1** can be further modified as

$$J_D \propto \frac{V_D}{L} exp\left[\frac{-\left(\phi_b - \sqrt{\frac{q^3 V_D}{L\pi\varepsilon_0\varepsilon_r}}\right)}{k_B T}\right] \qquad (2),$$

and a linear dependence of ln(J_D/V_D) on $V_D^{1/2}$ (see **Fig. S2 (b)**) suggests the dominance of a trap-induced Poole-Frenkel (PF) emission.

To better understand the impact of the traps on the carrier transport, the data is replotted in the log(J_D) versus log(V_D) curves (see **Fig. S2 (c)**). A current saturation occurs at V_D > 2 V for all the devices, implying a transition of the carrier transport from trap-filled limited (TFL) mode to space-charge limited (SCL) mode[36], and the current can be described as

$$J_D \propto \frac{1}{q^{m-2}}\left(\frac{2m-1}{m}\right)^m\left[\frac{\varepsilon_0\varepsilon_r(m-1)}{N_t m}\right]^{m-1}\frac{{V_D}^m}{L^{2m-1}} \quad (3),$$

where m is the power factor determined from the linear slope of the log(J_D) versus log(V_D) curves, and N_t is the trap density. In the TFL region (V_D < 2 V), the injected carriers are increased with V_D but not enough to fill the traps which have an exponential distribution[37,38]. In the SCL region (V_D > 2 V), all the traps are filled by the injected carriers, so the subsequently injected carriers are free from the traps and fully controlled by the space charges which limit further injection of the free carriers. The Cu-contact device has a slope (0.66) which is similar with the pristine one (0.62) but different from the Cu-doped one (0.06) in the trap-free SCL region. This result indicates that the SCL current is mainly determined by the channel material rather than the contact condition. Whereas in the TFL region, both the Cu-doped and Cu-contact devices show similar slopes (1.08 and 1.02) which are different from the pristine one (2.16), suggesting the impact of the Cu doping, either along the channel or at the contact interface, on the TFL current.

In the ln($J_D/{V_D}^2$) versus $1/V_D$ curves (see **Fig. S2 (d)**), the logarithmic dependence implies that the carrier transport is dominated by direct tunneling at the low temperature or thermionic emission (TE) at the high temperature. It can be predicted that by further increasing V_D, a linear decay would occur which corresponds to the Fowler-Nordheim (FN) tunneling through a triangular tunneling barrier and can be described by the following equation

$$J_D \propto \frac{q^3 m_0 {V_D}^2}{\phi_b L^2 m^*} exp\left[\frac{-8\pi\sqrt{2m^*}\,\phi_b^{\frac{3}{2}}L}{3hqV_D}\right] \quad (4).$$

Here m_0 is the free electron mass, m^* is the effective mass of electrons in WS_2, and h is the Planck's constant. To prevent the possible damage from the current-induced joule heating, in this work we limit the sweeping range of V_D only up to 5 V so the FN tunneling is excluded. The direct tunneling

through a trapezoidal tunneling barrier can be further confirmed by plotting the $\ln(J_D/V_D^2)$ versus $\ln(1/V_D)$ curves (see **Fig. S2 (e)**), based on the following equation

$$J_D \propto \frac{q^2 V_D \sqrt{m_0 \phi_b}}{h^2 L} exp\left[\frac{-4\pi\sqrt{m_0 \phi_b} L}{h}\right] \qquad (5).$$

The similar linear slopes of both the Cu-doped and Cu-contact devices indicate the comparable trapezoidal barrier heights at low V_D. Based on these analyses, we can conclude that the carrier injection at the low V_D ($V_D < 2$ V) is predominated by the thermionic emission or direct tunneling for all the devices, and the current is mainly attributed to the TFL current (see **Fig. S2 (f)**). At the high V_D ($V_D > 2$ V), the carrier injection is governed by the Schottky emission and the current is changed to the SCL current. The PF emission occurs at the low V_D for both the pristine and Cu-doped devices, but at the high V_D for the Cu-contact one.

Temperature dependence of the J_D-V_D output characteristics is measured from 218 to 298 K for each type of the devices, and a linear relation in the Arrhenius plot, i.e., $\ln(I_D/T^2)$ versus q/k_BT, is obtained for various V_G, as shown in **Fig. 2 (a)**. Our previous work has demonstrated a gate-dependent Schottky barrier modulation for 2D TMDs[39] and the value of ϕ_b for a given V_D is estimated from the slope of each curve, as shown in **Fig. 2 (b)**. At zero V_G or the equilibrium state, the value of ϕ_b is obtained as 166, 59, and 0 meV for the pristine, Cu-doped, and Cu-contact WS_2 devices, respectively. As V_G increases, a transition between the linear and exponential decay is observed, which indicates a flat-band condition across the metal-semiconductor interface. The carrier transport is dominated by the TE when $V_G < V_{FB}$, and by the direct tunneling or FN tunneling when $V_G > V_{FB}$, where V_{FB} is the flat-band gate voltage. The value of ϕ_b at V_{FB}, known as the intrinsic barrier height (ϕ_{b0}), can be used to estimate the band offsets between the metal and semiconductors. To further eliminate the effect from the applied V_D, ϕ_{b0} is plotted as a function of V_D, and the values at zero V_D are estimated based on a linear fit for each type of the devices, as

shown in **Fig. 2 (c)**. Compared to the pristine WS_2 FET (ϕ_{b0} = 123 meV), the value of ϕ_{b0} is

reduced to 89 meV for the Cu-doped WS_2 FET (i.e., ~28% reduction) and to 50 meV for the Cu-

contact WS_2 FET (i.e., ~60% reduction), suggesting a significant improvement of the metal-semiconductor contact condition. Our results are also compared with the theoretical barrier height calculated by density functional theory (DFT) for the monolayer WS_2 with various metal contacts[40], as shown in **Fig. 2 (d)**. The values obtained in this work are about one order of magnitude lower

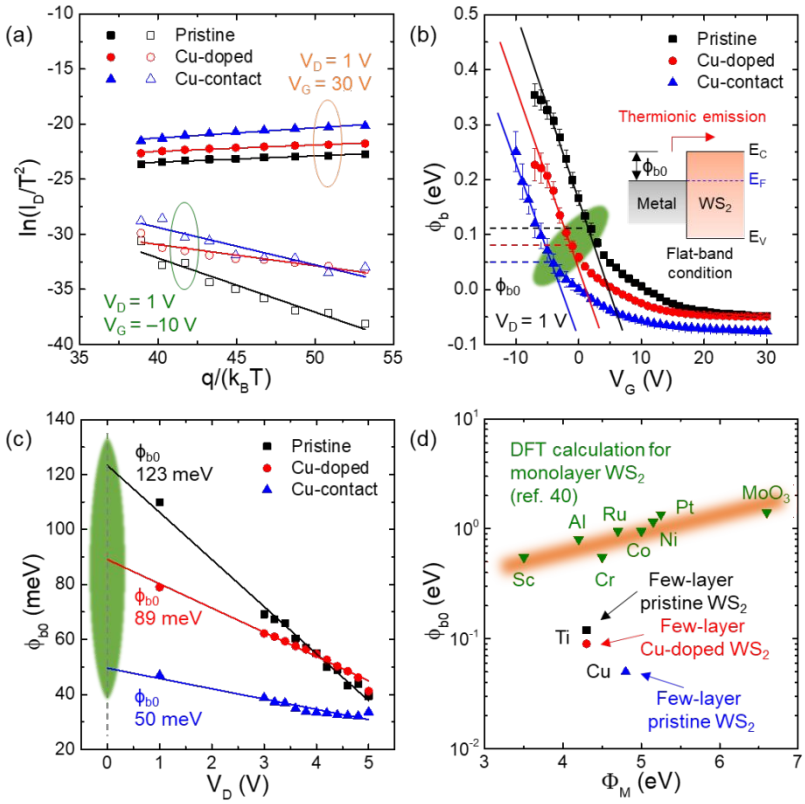

Fig. 2 Schottky barrier heights of WS_2 FETs. (a) The Arrhenius plots for on state (V_G = 30 V) and off state (V_G = –10 V) at V_D = 1 V. (b) The extracted ϕ_b as a function of V_G. The transition between linear and exponential decay highlighted in green indicates the flat-band condition at the metal-semiconductor interface. (c) The extracted ϕ_{b0} as a function of V_D. The values at zero V_D are predicted by a linear fit and highlighted in green. (d) Comparison of the experimentally extracted ϕ_{b0} with the theoretically calculated values for various metals.

due to the smaller bandgap in the multilayer structure.

Based on the extracted ϕ_{b0} at V_{FB} and ϕ_b at zero V_G, the band diagram of the metal-semiconductor interface can be estimated quantitatively, as shown in **Fig. 3**. Assuming that the work function of Ti (Φ_{Ti}) is 4.33 eV, the electron affinity for the pristine and Cu-doped WS_2 ($\chi_{WS2,pri}$ and $\chi_{WS2,Cu}$) can be calculated through ϕ_{b0} at V_{FB} as 4.21 and 4.24 eV, respectively. These two values are approximately identical as ideally the electron affinity is independent of the doping

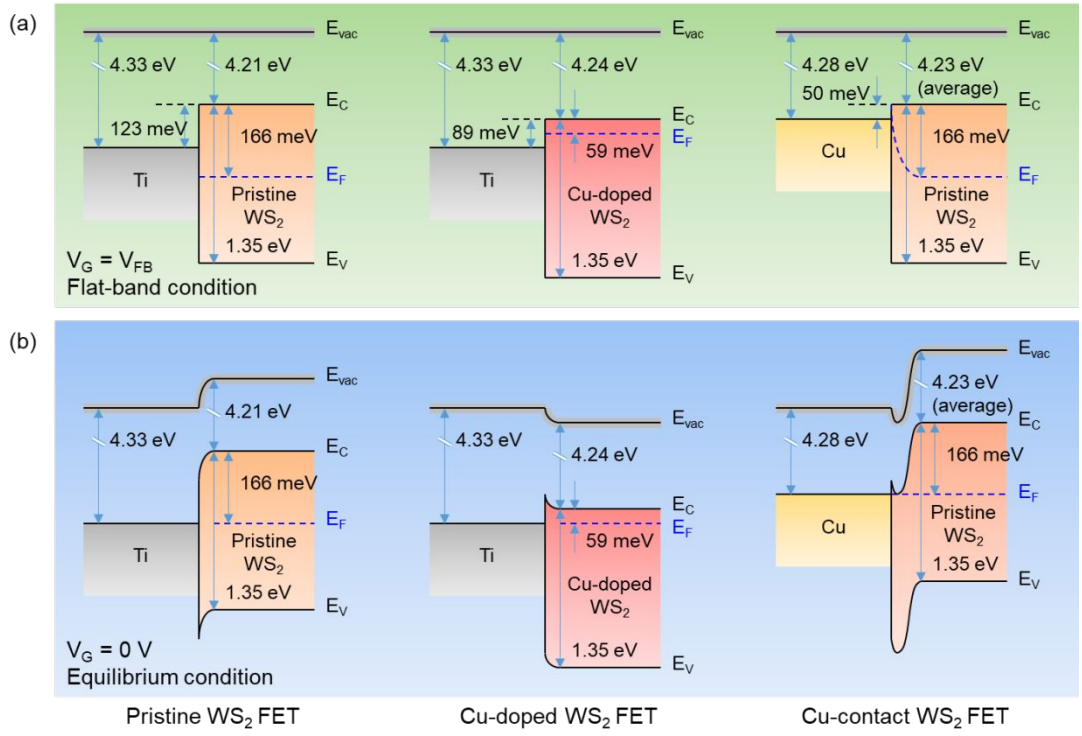

Fig. 3 Energy band diagram of the metal-semiconductor interface at zero V_D. (a) Energy band diagram at flat-band condition ($V_G = V_{FB}$). (b) Energy band diagram at equilibrium condition ($V_G = 0$ V). Here ϕ_{b0} at V_{FB} is measured to be 123, 89, and 50 meV, and ϕ_b at zero V_G is measured to be 166, 59, and 0 meV for the pristine, Cu-doped, and Cu-contact WS_2 FETs, respectively. E_{vac}, E_C, E_V, and E_F denote the vacuum energy level, the minima of the conduction band edge, the maxima of the valance band edge, and the Fermi energy level, respectively.

level. Therefore, we take their average value (4.23 eV) for the following discussion. At the equilibrium condition, the workfunction of the pristine and Cu-doped WS_2 ($\Phi_{WS2,pri}$ and $\Phi_{WS2,Cu}$) can be estimated as 4.4 and 4.29 eV, respectively. Therefore, the Schottky barrier lowering in the Cu-doped WS_2 FET can be interpreted by the electron doping which shifts the position of E_F close to E_C by about 0.11 eV (from 166 meV in the pristine WS_2 to 59 meV in the Cu-doped WS_2). Such n-type doping effect by Cu has also been reported on other 2D semiconducting materials[22,29]. As a comparison, the Schottky barrier lowering in the Cu-contact WS_2 FET is more complicated, which is mainly attributed to a synergetic interaction of exchange repulsion, covalent bonding, and charge redistribution including electron accumulation in the gap region, depletion near the interface, as well as charge density oscillations within both the metal and semiconductor[41]. Specifically, based on the average χ_{WS2} (4.23 eV) and ϕ_{b0} (50 meV) at V_{FB}, the work function of Cu (Φ_{Cu}) is estimated as 4.28 eV which is lower than the known value (4.69 eV, average of Cu (100), (110), and (111)) by about 0.41 eV. This unique decrease of Φ_{Cu} is in a good agreement with the previously theoretical predication, and can be attributed to the generation of a net interfacial dipole induced by the complex charge redistribution at the interface between Cu and group-VI TMDs[41]. Meanwhile, although the WS_2 bulk body remains pristine, $\Phi_{WS2,pri}$ at the interface is also reduced by contacting Cu due to the charge redistribution and surface dipole generation[41]. Thus, being different from the generalized Cu doping along the channel, the localized Cu contact leads to a strong n-type doping only at the contact surface, and gives rise to the zero ϕ_b at zero V_G. Besides, previous works have experimentally and theoretically demonstrated the great potential of WS_2 and other 2D TMDs acting as the Cu diffusion barrier[42,43], which also evidence that the doping effect induced by the Cu contact can be confined only at the contact interface.

Transfer characteristics. The comparison of J_D-V_G transfer characteristics at room temperature is shown in **Fig. 4 (a)**, from which it can be seen that the transistor performance, such as $J_{D,on}$, μ_{FE}, and SS are improved by introducing Cu as either the atomic dopants or the contact decoration. For example, the maximum $J_{D,on}$ of the pristine WS_2 FET at V_D of 1 V is 0.94 μA/μm, and this value is increased by about 5 times in the Cu-doped WS_2 FET (4.52 μA/μm) and by about 19 times in the Cu-contact WS_2 FET (17.73 μA/μm). The highest μ_{FE} for the Cu-doped WS_2 FET is 21.9 cm^2/Vs and for the Cu-contact WS_2 FET is 26.3 cm^2/Vs, which are more than 4 times larger than that of the pristine WS_2 device (4.9 cm^2/Vs). The lowest SS of the Cu-contact WS_2 FET is 0.5 V/decade which is about 70% reduced than that of the pristine and Cu-doped WS_2 devices. It is also noted that, even with the Cu atomic dopants in the semiconductor channel or the Cu contact decoration at the metal-semiconductor interface, no extra defects or traps are introduced in the devices. The effective trap density (n_t) can be estimated from the hysteresis of the charge neutral point (ΔV_{CNP}) as $n_t = C_{ox} \cdot \Delta V_{CNP}/q$, where C_{ox} is the oxide capacitance (3.84×10^{-8} F/cm^2 for a 90-nm-thick SiO_2 layer). Because all three types of the devices have the comparable values of ΔV_{CNP} from 13 to 17 V, the calculated n_t ranges from 3×10^{12} to 4×10^{12} cm^{-2}.

Based on the transfer characteristics, transconductance (g_m), defined as $g_m = \partial J_D/\partial V_G$ for a given V_D, is calculated and their temperature dependence indicates a metal-insulator transition (MIT) phenomenon, as shown in **Fig. 4 (b-d)**. Similar MIT behaviors in WS_2[44] and other TMDs such as MoS_2[45] and WSe_2[46] have also been reported previously with detailed experimental and theoretical investigation. Its origin can be attributed to the carrier transport environment including Coulomb impurities, charge traps and defects. The gate voltage required for inducing the MIT ($V_{G,MIT}$) in the pristine WS_2 FET is reduced from about 10 to 5 and 0 V by introducing Cu as the atomic dopant and contact decoration, respectively. The shift of $V_{G,MIT}$ to the negative V_G indicates

a Cu-induced n-type doping effect which is consistent with our previous discussion, and can be further interpreted by the frameworks of thermally activated and variable-range hopping (VRH) models[14]. For example, activation energy (E_a) which is corresponding to the thermal activation of charge carriers into the conduction band is extracted by fitting the sheet conductivity (G) with the expression $G(T) = G_0\exp(-E_a/k_BT)$, where G_0 is the constant. A plot of $\ln(G)$ versus $1000/T$ at the on state for each type of the devices is shown in **Fig. 4 (e)**. The values of E_a are extracted from the linear fit of the plots, and their dependence on V_G across the subthreshold and superthreshold regions (–10 to 30 V) are calculated, as shown in **Fig. 4 (f)**. A clear reduction of E_a can be found in the Cu-doped and Cu-contact WS_2 FETs, which is consistent with the behavior of the V_G-dependent ϕ_b (see **Fig. 2 (b)**). Assuming the dependence of E_a on V_G equals to the dependence of E_F on V_G, the density of the states (DOS) below the conduction band edge can be extracted from the expression $dE_F/\mathrm{d}V_G = dE_a/dV_G = C_{ox}/(C_{ox}+C_t)$, where $C_t = e^2DOS$ is the quantum capacitance. **Figure 4 (g)** shows the calculated DOS as a function of V_G across the insulating and metallic regimes in a comparison with the theoretically anticipated value of DOS ($DOS_{2D,theory}$) which equals to 2.85×10^{14} $eV^{-1}cm^{-2}$ at the effective mass $m^* = 0.34\ m_0$[7,14]. The average DOS is increased from 10^{12} to 10^{14} $eV^{-1}cm^{-2}$ when V_G increases from the subthreshold region to the superthreshold region. Based on the VRH model[47-49], the localization length L_{local} is calculated as $L_{local} = (13.8/k_BT_0DOS)^{1/2}$, where T_0 is the temperature coefficient to describe the temperature dependence of G as $G(T) \sim \exp(-T_0/T)^{1/3}$. **Figure 4 (h)** shows that, with the increasing V_G, the electron delocalization occurs and the localization length can reach up to about hundreds of nanometers. Compared to the pristine WS_2 FET, both the Cu doping and Cu contact can initiate the delocalization process at lower V_G and potentially benefit the low-power energy-efficient device applications.

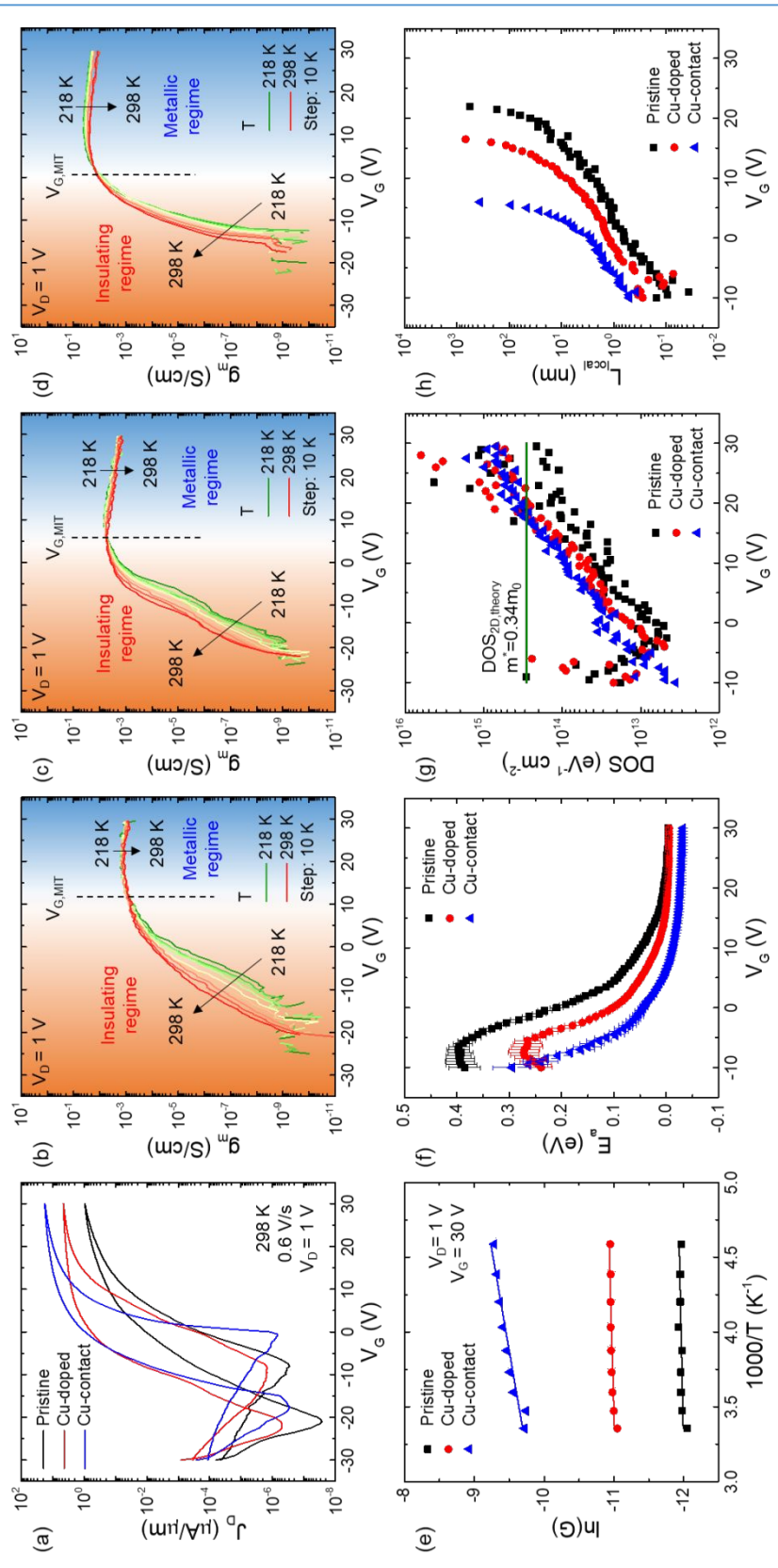

Fig. 4 Comparison of transfer characteristics of WS_2 FETs and *IV* characteristics based on the transfer curves. (a) Comparison of transfer characteristics at room temperature for the pristine, Cu-doped, and Cu-contact WS_2 FETs. (b-d) The extracted g_m as a function of V_G at various T illustrates the MIT effect in the pristine, Cu-doped, and Cu-contact WS_2 FETs, respectively. The insulating and metallic regimes are colored in orange and blue. (e, f) A plot of $\ln(G)$ versus $1000/T$ shows the extraction of E_a from a linear fit at $V_D = 1$ V and $V_G = 30$ V, and the extracted E_a as a function of V_G for all three types of the devices. (g, h) The extracted *DOS* and L_{local} as the functions of V_G for all three types of the devices.

Being consistent with the MIT behavior, the electron currents (e.g., at V_G = 30 V or the on state) for all three types of the devices decrease with T from 218 to 298 K, whereas the hole currents (e.g., at V_G = –30 V or the off state) increase with T, as shown in **Fig. 5 (a)**. The T-dependent electron current variation can be attributed to the dominance of lattice scattering which decreases μ_{FE} with the increasing T. Here μ_{FE} is defined as $(L/W)(1/C_{ox})(1/V_D)g_m$ where L and W are the channel length and width, respectively. It is found that μ_{FE} follows a power-law relation with T as $\mu_{FE} \sim T^{-\gamma}$, where γ is the temperature damping factor and calculated to be 0.7, 0.72, and 1.66 for the pristine, Cu-doped, and Cu-contact WS_2 FETs, respectively, as shown in **Fig. 5 (b)**. Our results show a good agreement with previous reports on the WS_2 FETs where the value of γ ranges from 0.73 to 1.75[14]. On the other hand, the hole currents increase with T due to the thermal energy assisted generation of the minority charge carriers which contribute to the leakage current at the off state.

To further confirm the enhancement of the carrier injection through the metal-semiconductor contact interface, we fabricate transmission line measurement (TLM) devices to extract the contact resistance (R_C) as a function of V_G for each type of the devices, as shown in **Fig. 5 (c)** as well as **Fig. S1** and **S3** in Supplementary Information. At the on state, R_C is calculated as 2.2×10^9, 7.4×10^6, and 1×10^6 Ωμm for the pristine, Cu-doped, and Cu-contact WS_2 FETs, respectively, suggesting a significant improvement (a reduction by about three orders of magnitude) of the carrier injection by introducing Cu. Even at the off state, R_C also shows a reduction by one order of the magnitude with either the Cu atomic doping or Cu contact decoration. Our results are also benchmarked as a function of the channel resistivity, $\rho_{2D,channel} = (R_{total}–R_C)W/L$[34], in a comparison with the merit of the monolayer WS_2[14] and few-layer Cl-doped WS_2[50], as shown in **Fig. 5 (d)**. Here R_{total} is the total resistance measured as V_D/J_D. It is noted that both the Cu atomic

doping and Cu contact decoration can provide the lowest R_C/R_{total} ratio which is required to be 20% by the International Technology Roadmap for Semiconductors (ITRS) in 2015.

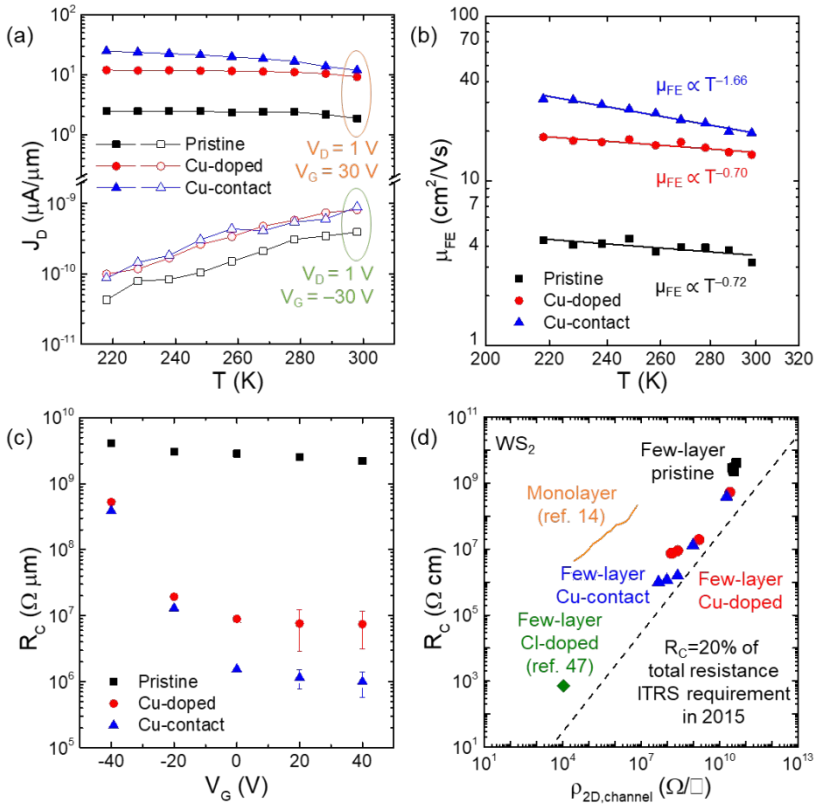

Fig. 5 Carrier mobility and contact resistance of WS_2 FETs. (a, b) J_D as a function of T and μ_{FE} as a function of log(T) for each type of the devices. (c) The extracted R_C as a function of V_G with error bars at the on-state. (d) Benchmarking of the extracted R_C as a function of $\rho_{2D,channel}$ in a comparison with monolayer and few-layer Cl-doped WS_2. The dashed line depicts the criterion R_C = 20% of total resistance in a transistor with a 22-nm-long gate as required by ITRS in 2015.

To minimize and eliminate the possible deviation among the devices due to the variations in terms of the flake uniformity, contaminations, and contact conditions etc., a statistical analysis

based on about 30 devices of each type is carried out at room temperature, which proves the reliability and accuracy of our results. Under the same measurement condition, the J_D-V_G transfer characteristics of all the pristine, Cu-doped, and Cu-contact WS_2 FETs are compared, as shown in **Fig. S4** in Supplementary Information. The statistical analysis of the transistor performance, including μ_{FE}, $J_{D,on}$, on/off ratio, and SS, are summarized in **Fig. 6**. Both the median and mean values show a clear improvement by introducing the Cu atomic doping and Cu contact decoration. For example, compared to the pristine WS_2 FETs, the mean values of μ_{FE}, $J_{D,on}$, and on/off ratio in the Cu-doped WS_2 FETs are about 5, 4, and 2 times increased, respectively, and the mean value of SS is over 30% reduced. The Cu-contact WS_2 FETs show an even better performance, including about 7 times increases in μ_{FE} and $J_{D,on}$, 6 times increases in on/off ratio, and 26% reduction in SS.

Although an n-type doping effect from Cu atomic doping and Cu contact decoration is anticipated, the threshold voltage (V_{th}) for the Cu-doped and Cu-contact WS_2 FETs in this work doesn't show a clear and noticeable shift toward positive V_G through the statistical analysis, in a comparison with the pristine WS_2 FETs. The absence of the V_{th} shift can be interpreted by the low concentration of Cu dopants in the Cu-doped devices and the localization of Cu doping region in the Cu-contact devices. For the Cu atomic doping, the actual Cu dopant concentration after synthesis was very low, which was only 3% in the weight ratio confirmed by energy-dispersive X-ray spectroscopy (EDX, see Methods). The Raman shift indicated a very small red shift of the A^1_g mode (from 422.5 to 421.9 cm^{-1}) which also suggests a relatively weak doping effect (see Methods and **Fig. S5** in Supplementary Information). Therefore, the shift of V_{th} in the Cu-doped FETs is not clear or noticeable in this work. For the Cu contact decoration, the doping effect was only introduced locally at the source and drain contact interfaces. The transistor operation still relies on the carrier transport by thermionic emission over the potential barrier in the channel, and the

channel remains the same as the pristine WS_2. Therefore, such localized doping near the contacts won't significantly cause the shift of V_{th}, in a comparison with the pristine WS_2 FETs.

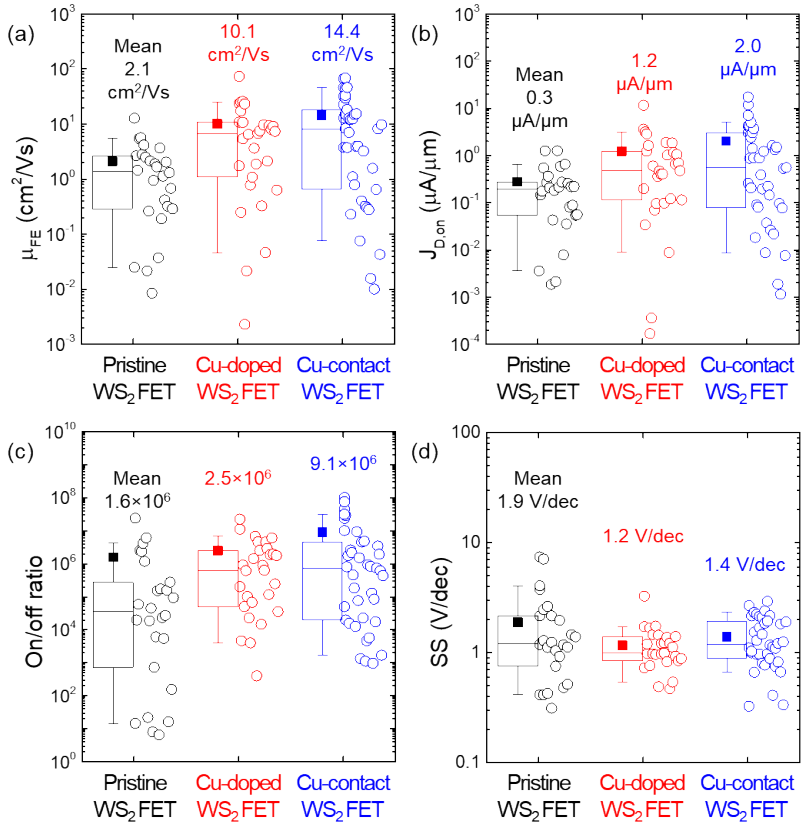

Fig. 6 Statistical analysis of transistor performance for 26 pristine WS_2 FETs, 29 Cu-doped WS_2 FETs, and 39 Cu-contact WS_2 FETs. (a-d) Comparison of transistor performance including μ_{FE}, $J_{D,on}$, on/off ratio, and SS, respectively. Here the box ranges from 25 to 75 percentile and the whisker ranges from 10 to 90 percentile. The bar in the box and the solid square denote the median and mean values, respectively.

CONCLUSIONS

We carry out a comparative study among the pristine, Cu-doped, and Cu-contact WS_2 FETs, and demonstrate that both the Cu atomic doping and Cu contact decoration can efficiently enhance the

carrier transport in WS_2 FETs. The charge transfer with Cu can effectively change the Fermi level of WS_2 along the channel for the Cu-doped devices, and considerably reduce the workfunction of Cu at the metal-semiconductor interface for the Cu-contact devices. The Schottky-to-Ohmic contact transition with the lowered contact barrier can enhance the carrier injection through the metal-semiconductor interface, and give rise to the drastic reduction of R_C. The statistical analysis shows a significant improvement of the carrier transport as well as the device performance in terms of μ_{FE}, $J_{D,on}$, on/off ratio, and SS.

METHODS

Material synthesis and characterization. Both the pristine WS_2 and Cu-doped WS_2 crystals were grown by chemical vapor transport (CVT) reaction using iodine as a transport agent. A slow growth rate from the vapor phase ensures an extremely low density of structural defects in crystals, based on our previous studies[51-54]. Briefly, a silica ampoule containing WS_2 powder and iodine were evacuated and sealed at a pressure of 10^{-3} Pa to synthesis the pristine WS_2. The transport reaction ran at 1060 K with a temperature gradient of 5.6 K/cm in a two-zone furnace. After three weeks of growth, the silica ampoule was slowly cooled to room temperature with a controlled cooling rate of 15 K per hour. Approximately a few percent of the starting material were transported by the reaction to form nanotube structures, and the rest of the transported material grows thin layered crystals. For the Cu-doped WS_2, the growth followed the same procedure but a small amount of Cu foil (0.5% by nominal weight) were added in the ampoule. Then, both the pristine and Cu-doped WS_2 flakes were mechanically exfoliated from the synthesized crystals and transferred onto n-type Si substrates (0.001-0.005 Ωcm) which had a 90-nm-thick SiO_2 layer on the top. An EDX characterization was carried out to verify the existence

of Cu in the synthesized WS_2 flakes, as shown in **Fig. S5 (a)** and **(b)** in Supplementary Information. The Cu-doped WS_2 showed a uniform distribution of Cu, and the weight ratio (or atomic ratio) of W/S/Cu was measured as 0.67/0.22/0.03 (or 0.30/0.57/0.04), in addition to O, C, and I in the sample. As a comparison, the pristine WS_2 has the weight ratio (or atomic ratio) of W/S as 0.71/0.28 (or 0.30/0.67). Both the synthesized pristine and Cu-doped WS_2 were also investigated by Raman spectroscopy, as shown in **Fig. S5 (c-e)** in Supplementary Information. Compared to the monolayer WS_2, both the peak positions and intensity ratios[55] indicated the few-layer structures of the pristine and Cu-doped WS_2 flakes in this work. Moreover, the E^1_{2g} peaks for the pristine and Cu-doped WS_2 were located consistently at around 357 cm^{-1}, suggesting a negligible effort of Cu atomic doping on the in-plane vibrational mode of WS_2. In contrast, the A^1_g peak was found to be softened (red-shifted) from 422.5 to 421.9 cm^{-1} due to the Cu-induced electron doping. The insensitivity of the E^1_{2g} peak and the pronounced red-shift of the A^1_g peak were consistent with the sign of electron doping on other TMD semiconductors such as MoS_2[56].

Device fabrication and measurement. For a comparative study, we fabricated three types of typical global-back-gate transistors: the pristine, Cu-doped, and Cu-contact WS_2 FETs. Both the pristine and Cu-doped WS_2 FETs had Ti/Au (10 nm/100 nm) deposited as source and drain electrodes. The Cu-contact WS_2 FETs had Cu/Ti/Au (2 nm/10 nm/100 nm) as the electrodes on the pristine WS_2 flakes where the thin Cu layer serves as a contact decoration at the metal-semiconductor interface. All the pristine and Cu-doped WS_2 flakes had the similar thickness (t) ranging from 4 to 8 nm, measured by atomic force microscopy (AFM). In this thickness range, all the flakes were assumed to behave like bulk crystals with a consistent bandgap[57]. The value of L was set as 1 μm for all the FETs but the values of W were varying for each device. The AFM data of a selected Cu-doped WS_2 FET was shown in **Fig. S6** in Supplementary Information, where t, L,

and W were measured to be 6 nm, 1 μm, and 4 μm, respectively. The electrical characterization was performed by measuring drain current (I_D) at various V_D and V_G, and the value of I_D was further normalized to J_D ($J_D = I_D/W$) for performance comparison. The room-temperature measurement was performed in a dark N_2-filled ambient environment, and the low-temperature measurement was carried out in a vacuum environment (~2 mTorr).

ASSOCIATED CONTENT

Supporting Information

AUTHOR INFORMATION

Corresponding authors

whwang@kau.ac.kr, feiyao@buffalo.edu, huaminli@buffalo.edu

Author contributions

W.H., F.Y., and H.L. conceived and supervised the project. M.R. synthesized the 2D crystals. P.P. and S.F. prepared the 2D thin flakes. W.H. fabricated the 2D transistor devices. M.L. and P.P. fabricated the 2D TLM devices. M.L., S.S., H.N.J., and H.L. performed the electrical characterizations. M.L., S.W., F.Y., and J.J. performed the material characterizations.

Acknowledgements

This work was partially supported by the National Science Foundation (NSF) under Award ECCS-1944095, the New York State Energy Research and Development Authority (NYSERDA) under

Award 138126, and the New York State Center of Excellence in Materials Informatics (CMI) under Award C160186.

Ethics declarations

The authors declare no competing interests.

REFERENCES

(1) Yang, L.; Sinitsyn, N. A.; Chen, W.; Yuan, J.; Zhang, J.; Lou, J.; Crooker, S. A. Long-Lived Nanosecond Spin Relaxation and Spin Coherence of Electrons in Monolayer MoS_2 and WS_2. *Nat. Phys.* **2015**, *11*, 830–834.

(2) Zeng, H.; Liu, G.-B.; Dai, J.; Yan, Y.; Zhu, B.; He, R.; Xie, L.; Xu, S.; Chen, X.; Yao, W.; *et al.* Optical Signature of Symmetry Variations and Spin-Valley Coupling in Atomically Thin Tungsten Dichalcogenides. *Sci. Rep.* **2013**, *3*.

(3) Britnell, L.; Ribeiro, R. M.; Eckmann, A.; Jalil, R.; Belle, B. D.; Mishchenko, A.; Kim, Y.-J.; Gorbachev, R. V.; Georgiou, T.; Morozov, S. V.; *et al.* Strong Light-Matter Interactions in Heterostructures of Atomically Thin Films. *Sci.* **2013**, *340*, 1311–1314.

(4) Braga, D.; Lezama, I. G.; Berger, H.; Morpurgo, A. F. Quantitative Determination of the Band Gap of WS_2 with Ambipolar Ionic Liquid-Gated Transistors. *Nano Lett.* **2012**, *12*, 5218–5223.

(5) Gusakova, J.; Wang, X.; Shiau, L. L.; Krivosheeva, A.; Shaposhnikov, V.; Borisenko, V.; Gusakov, V.; Tay, B. K. Electronic Properties of Bulk and Monolayer TMDs: Theoretical Study Within DFT Framework (GVJ-2e Method). *Phys. Status Solidi (a)* **2017**, *214*, 1700218.

(6) Klein, A.; Tiefenbacher, S.; Eyert, V.; Pettenkofer, C.; Jaegermann, W. Electronic Band Structure of Single-Crystal and Single-layerWS_2: Influence of Interlayer Van Der Waals Interactions. *Phys. Rev. B* **2001**, *64*.

(7) Liu, L.; Kumar, S. B.; Ouyang, Y.; Guo, J. Performance Limits of Monolayer Transition Metal Dichalcogenide Transistors. *IEEE Trans. Electron Devices* **2011**, *58*, 3042–3047.

(8) Chen, K.-T.; Chang, S.-T. How High Can the Mobility of Monolayer Tungsten Disulfide Be? *Vacuum* **2017**, *140*, 172–175.

(9) Zhang, W.; Huang, Z.; Zhang, W.; Li, Y. Two-Dimensional Semiconductors with Possible High Room Temperature Mobility. *Nano Res.* **2014**, *7*, 1731–1737.

(10) Iqbal, M. W.; Iqbal, M. Z.; Khan, M. F.; Shehzad, M. A.; Seo, Y.; Park, J. H.; Hwang, C.; Eom, J. High-Mobility and Air-Stable Single-Layer WS_2 Field-Effect Transistors Sandwiched between Chemical Vapor Deposition-Grown Hexagonal BN Films. *Sci. Rep.* **2015**, *5*.

(11) Cui, Y.; Xin, R.; Yu, Z.; Pan, Y.; Ong, Z.-Y.; Wei, X.; Wang, J.; Nan, H.; Ni, Z.; Wu, Y.; *et al.* High-Performance Monolayer WS_2 Field-Effect Transistors on High-κ Dielectrics. *Adv. Mater.* **2015**, *27*, 5230–5234.

(12) Illarionov, Y. Y.; Molina-Mendoza, A.; Waltl, M.; Knobloch, T.; Furchi, M.; Mueller, T.; Grasser, T. Reliability of next-Generation Field-Effect Transistors with Transition Metal Dichalcogenides. *2018 IEEE Int. Reliab. Phys. Symp. (IRPS)* **2018**.

(13) Yue, Y.; Chen, J.; Zhang, Y.; Ding, S.; Zhao, F.; Wang, Y.; Zhang, D.; Li, R.; Dong, H.; Hu, W.; *et al.* Two-Dimensional High-Quality Monolayered Triangular WS_2 Flakes for Field-Effect Transistors. *ACS Appl. Mater. Interfaces* **2018**, *10*, 22435–22444.

(14) Ovchinnikov, D.; Allain, A.; Huang, Y.-S.; Dumcenco, D.; Kis, A. Electrical Transport Properties of Single-Layer WS_2. *ACS Nano* **2014**, *8*, 8174–8181.

(15) Liu, X.; Hu, J.; Yue, C.; Fera, N. D.; Ling, Y.; Mao, Z.; Wei, J. High Performance Field-Effect Transistor Based on Multilayer Tungsten Disulfide. *ACS Nano* **2014**, *8*, 10396–10402.

(16) Kumar, J.; Kuroda, M. A.; Bellus, M. Z.; Han, S.-J.; Chiu, H.-Y. Full-Range Electrical Characteristics of WS_2 Transistors. *Appl. Phys. Lett.* **2015**, *106*, 123508.

(17) Georgiou, T.; Jalil, R.; Belle, B. D.; Britnell, L.; Gorbachev, R. V.; Morozov, S. V.; Kim, Y.-J.; Gholinia, A.; Haigh, S. J.; Makarovsky, O.; *et al.* Vertical Field-Effect Transistor Based on Graphene–WS_2 Heterostructures for Flexible and Transparent Electronics. *Nat. Nanotechnol.* **2012**, *8*, 100–103.

(18) Wang, J.; Jia, R.; Huang, Q.; Pan, C.; Zhu, J.; Wang, H.; Chen, C.; Zhang, Y.; Yang, Y.; Song, H.; *et al.* Vertical WS_2/SnS_2 Van Der Waals Heterostructure for Tunneling Transistors. *Sci. Rep.* **2018**, *8*.

(19) Tedstone, A. A.; Lewis, D. J.; Obrien, P. ChemInform Abstract: Synthesis, Properties, and Applications of Transition Metal-Doped Layered Transition Metal Dichalcogenides. *Chem. Inform.* **2016**, *47*.

(20) Luo, P.; Zhuge, F.; Zhang, Q.; Chen, Y.; Lv, L.; Huang, Y.; Li, H.; Zhai, T. Doping Engineering and Functionalization of Two-Dimensional Metal Chalcogenides. *Nanoscale Horiz.* **2019**, *4*, 26–51.

(21) Sun, H.; Shang, Y.; Yang, Y.; Guo, M. Realization of N-Type Semiconducting of Phosphorene through Surface Metal Doping and Work Function Study. *J. Nanomater.* **2018**, *2018*, 1–9.

(22) Koenig, S. P.; Doganov, R. A.; Seixas, L.; Carvalho, A.; Tan, J. Y.; Watanabe, K.; Taniguchi, T.; Yakovlev, N.; Neto, A. H. C.; Özyilmaz, B. Electron Doping of Ultrathin Black Phosphorus with Cu Adatoms. *Nano Lett.* **2016**, *16*, 2145–2151.

(23) Liu, Y.; Babu, H. V.; Zhao, J.; Goñi-Urtiaga, A.; Sainz, R.; Ferritto, R.; Pita, M.; Wang, D.-Y. Effect of Cu-Doped Graphene on the Flammability and Thermal Properties of Epoxy Composites. *Composites, Part B.* **2016**, *89*, 108–116.

(24) Yun, W. S.; Lee, J. D. Unexpected Strong Magnetism of Cu Doped Single-Layer MoS_2 and Its Origin. *Phys. Chem. Chem. Phys.* **2014**, *16*, 8990–8996.

(25) Hu, A.-M.; Wang, L.-L.; Xiao, W.-Z.; Meng, B. Electronic Structures and Magnetic Properties in Cu-Doped Two-Dimensional Dichalcogenides. *Phys. E* **2015**, *73*, 69–75.

(26) Koski, K. J.; Wessells, C. D.; Reed, B. W.; Cha, J. J.; Kong, D.; Cui, Y. Chemical Intercalation of Zerovalent Metals into 2D Layered Bi_2Se_3 Nanoribbons. *J. Am. Chem. Soc.* **2012**, *134*, 13773–13779.

(27) Koski, K. J.; Cha, J. J.; Reed, B. W.; Wessells, C. D.; Kong, D.; Cui, Y. High-Density Chemical Intercalation of Zero-Valent Copper into Bi_2Se_3 Nanoribbons. *J. Am. Chem. Soc.* **2012**, *134*, 7584–7587.

(28) Chen, K. P.; Chung, F. R.; Wang, M.; Koski, K. J. Dual Element Intercalation into 2D Layered Bi_2Se_3 Nanoribbons. *J. Am. Chem. Soc.* **2015**, *137*, 5431–5437.

(29) Muhammad, Z.; Mu, K.; Lv, H.; Wu, C.; Rehman, Z. U.; Habib, M.; Sun, Z.; Wu, X.; Song, L. Electron Doping Induced Semiconductor to Metal Transitions in $ZrSe_2$ Layers via Copper Atomic Intercalation. *Nano Res.* **2018**, *11*, 4914–4922.

(30) Wu, X.; Han, J.; Feng, Y.; Li, G.; Wang, C.; Ding, G.; Gao, G. Half-Metals and Half-Semiconductors in a Transition Metal Doped $SnSe_2$ Monolayer: a First-Principles Study. *RSC Adv.* **2017**, *7*, 44499–44504.

(31) Wang, F.; Zhou, L.; Ma, Z.; He, M.; Wu, F.; Liu, Y. First-Principles Investigations of Magnetic Semiconductors: An Example of Transition Metal Decorated Two-Dimensional SnS Monolayer. *Nanomater.* **2018**, *8*, 789.

(32) Zhao, X.; Dai, X.; Xia, C. Magnetic Properties of Two Nearest Cu-Doped Monolayer WS_2: A First-Principles Study. *Solid State Commun.* **2015**, *217*, 66–69.

(33) Franklin, A. D. Nanomaterials in Transistors: From High-Performance to Thin-Film Applications. *Sci.* **2015**, *349*.

(34) Allain, A.; Kang, J.; Banerjee, K.; Kis, A. Electrical Contacts to Two-Dimensional Semiconductors. *Nat. Mater.* **2015**, *14*, 1195–1205.

(35) Kong, Z.; Liu, D.; He, J.; Wang, X. Electrode Buffer Layers Producing High Performance Nonvolatile Organic Write-Once-Read-Many-Times Memory Devices. *RSC Adv.* **2017**, *7*, 13171–13176.

(36) Shin, Y. S.; Lee, K.; Kim, Y. R.; Lee, H.; Lee, I. M.; Kang, W. T.; Lee, B. H.; Kim, K.; Heo, J.; Park, S.; *et al.* Mobility Engineering in Vertical Field Effect Transistors Based on Van Der Waals Heterostructures. *Adv. Mater.* **2018**, *30*, 1704435.

(37) Qu, D.; Liu, X.; Ahmed, F.; Lee, D.; Yoo, W. J. Self-Screened High Performance Multi-Layer MoS_2transistor Formed by Using a Bottom Graphene Electrode. *Nanoscale* **2015**, *7*, 19273–19281.

(38) Ghatak, S.; Ghosh, A. Observation of Trap-Assisted Space Charge Limited Conductivity in Short Channel MoS_2 Transistor. *Appl. Phys. Lett.* **2013**, *103*, 122103.

(39) Li, H.-M.; Lee, D.-Y.; Choi, M. S.; Qu, D.; Liu, X.; Ra, C.-H.; Yoo, W. J. Metal-Semiconductor Barrier Modulation for High Photoresponse in Transition Metal Dichalcogenide Field Effect Transistors. *Sci. Rep.* **2014**, *4*.

(40) Guo, Y.; Liu, D.; Robertson, J. 3D Behavior of Schottky Barriers of 2D Transition-Metal Dichalcogenides. *ACS Appl. Mater. Interfaces* **2015**, *7*, 25709–25715.

(41) Helfrecht, B. A.; Guzman, D. M.; Onofrio, N.; Strachan, A. H. Interactions between Copper and Transition Metal Dichalcogenides: A Density Functional Theory Study. *Phys. Rev. Mater.* **2017**, *1*.

(42) Smithe, K. K. H.; Zhu, Z.; Bailey, C. S.; Pop, E.; Yoon, A. Investigation of Monolayer MX_2 as Sub-Nanometer Copper Diffusion Barriers. *2018 IEEE Int. Reliab. Phys. Symp. (IRPS)* **2018**.

(43) Lo, C.-L.; Catalano, M.; Smithe, K. K. H.; Wang, L.; Zhang, S.; Pop, E.; Kim, M. J.; Chen, Z. Studies of Two-Dimensional h-BN and MoS_2 for Potential Diffusion Barrier Application in Copper Interconnect Technology. *npj 2D Mater. Appl.* **2017**, *1*.

(44) Cui, Y.; Xin, R.; Yu, Z.; Pan, Y.; Ong, Z.-Y.; Wei, X.; Wang, J.; Nan, H.; Ni, Z.; Wu, Y.; Chen, T.; Shi, Y.; Wang, B.; Zhang, G.; Zhang, Y.-W.; Wang, X. High-performance monolayer WS_2 field-effect transistors on high-k dielectrics. *Adv. Mater.* **2015**, 27, 5230.

(45) Radisavljevic, B.; Kis, A. Mobility engineering and a metal-insulator transition in monolayer MoS_2. *Nat. Mater.* **2013**, 12, 815.

(46) Allain, A.; Kis, A. Electron and hole mobilitis in single-layer WSe_2. *ACS Nano* **2014**, 8, 7180.

(47) Jonscher, A. Electronic Processes in Non-Crystalline Materials. *Thin Solid Films* **1972**, *11*, 439–440.

(48) Keuls, F. W. V.; Hu, X. L.; Jiang, H. W.; Dahm, A. J. Screening of the Coulomb Interaction in Two-Dimensional Variable-Range Hopping. *Phys. Rev B* **1997**, *56*, 1161–1169.

(49) Ghatak, S.; Pal, A. N.; Ghosh, A. Nature of Electronic States in Atomically Thin MoS_2 Field-Effect Transistors. *ACS Nano* **2011**, *5*, 7707–7712.

(50) Yang, L.; Majumdar, K.; Liu, H.; Du, Y.; Wu, H.; Hatzistergos, M.; Hung, P. Y.; Tieckelmann, R.; Tsai, W.; Hobbs, C.; *et al.* Chloride Molecular Doping Technique on 2D Materials: WS_2 and MoS_2. *Nano Lett.* **2014**, *14*, 6275–6280.

(51) Hwang, W. S.; Remskar, M.; Yan, R.; Protasenko, V.; Tahy, K.; Chae, S. D.; Zhao, P.; Konar, A.; Xing, H. (G.; Seabaugh, A.; *et al.* Transistors with Chemically Synthesized Layered Semiconductor WS_2 Exhibiting 105 Room Temperature Modulation and Ambipolar Behavior. *Appl. Phys. Lett.* **2012**, *101*, 013107.

(52) Remìkar, M.; Škraba, Z.; Regula, M.; Ballif, C.; Sanjinés, R.; Lévy, F. New Crystal Structures of WS_2: Microtubes, Ribbons, and Ropes. *Adv. Mater.* **1998**, *10*, 246–249.

(53) Viršek, M.; Jesih, A.; Milošević, I.; Damnjanović, M.; Remškar, M. Raman Scattering of the MoS_2 and WS_2 Single Nanotubes. *Surf. Sci.* **2007**, *601*, 2868–2872.

(54) Krause, M.; Viršek Marko; Remškar Maja; Salacan, N.; Fleischer, N.; Chen, L.; Hatto, P.; Kolitsch, A.; Möller, W. Diameter and Morphology Dependent Raman Signatures of WS_2 Nanostructures. *ChemPhysChem* **2009**, *10*, 2221–2225.

(55) Berkdemir, A.; Gutiérrez, H. R.; Botello-Méndez, A. R.; Perea-López, N.; Elías, A. L.; Chia, C.-I.; Wang, B.; Crespi, V. H.; López-Urías, F.; Charlier, J.-C.; *et al.* Identification of Individual and Few Layers of WS_2 Using Raman Spectroscopy. *Sci. Rep.* **2013**, *3*.

(56) Chakraborty, B.; Bera, A.; Muthu, D. V. S.; Bhowmick, S.; Waghmare, U. V.; Sood, A. K. Symmetry-Dependent Phonon Renormalization in Monolayer MoS_2 Transistor. *Phys. Rev. B* **2012**, *85*.

(57) Cao, Q.; Dai, Y.-W.; Xu, J.; Chen, L.; Zhu, H.; Sun, Q.-Q.; Zhang, D. W. Realizing stable p-type transporting in two-dimensional WS_2 films. *ACS Appl. Mater. Interfaces* **2017**, 9, 18215.

Table of Content Graphic